Article

4D Printed Shape Memory Polyurethane-Based Composite for Bionic Cartilage Scaffolds

Yongdie Deng, Fenghua Zhang, Yanju Liu, Shiqi Zhang, Huiping Yuan, and Jinsong Leng*

Cite This: *ACS Appl. Polym. Mater.* 2023, 5, 1283−1292

Read Online

ACCESS | Metrics & More | Article Recommendations | Supporting Information

ABSTRACT: Repair of articular cartilage defects is a major challenge in orthopedic surgery due to the deficient self-regeneration capability. Cartilage tissue engineering scaffolds provide a promising approach to cartilage defect repair. Proper mechanical properties, interconnected internal structure, customized shape, and minimally invasive treatment are urgent requirements for a qualified cartilage scaffold. Here, a shape memory composite used for cartilage defects is prepared by adding nanohydroxyapatite into a shape memory polyurethane matrix, exhibiting good mechanical properties and biocompatibility. Based on its rheological properties, the composite melt can be printed into 4D printed structures with high precision and quality in a simple and clean way. Inspired by the structure of mangroves, a bionic 4D printed cartilage scaffold is designed and manufactured, presenting a good shape memory performance at a temperature close to body temperature. The 4D printed cartilage scaffold can expand from a conveniently insertional shape to a deployed shape to match defect, providing a novel idea for the personalized and minimally invasive treatment of cartilage defects.

KEYWORDS: 4D printing, shape memory composites, polyurethane, bionic scaffold, cartilage defects
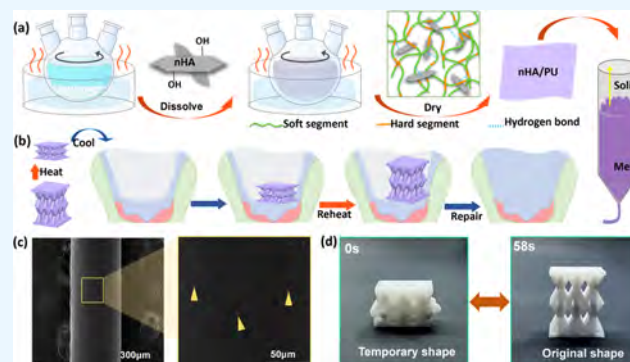
1. INTRODUCTION

Articular cartilage on the bone−bone contact surface possesses rigid and elastic mechanical properties, providing a smooth surface to support the joint motion and assist the load transmission through it.[1] Currently, cartilage defects caused by trauma and degenerative osteoarthritis are common diseases in orthopedics.[2] Repair of cartilage defects is a major challenge in orthopedic surgery due to the lack of intrinsic deficiency of self-regeneration capability. Cartilage tissue engineering scaffolds are considered as an appropriate platform for cell adhesion, proliferation, and differentiation, providing another promising approach for cartilage defect repair.[3,4] The scaffold material and structure play an essential role in promoting cartilage regeneration while ensuring biocompatibility and mechanical properties. The cartilage scaffold materials should have good histocompatibility, biodegradability, and mechanical properties. In recent years, some natural polymers such as silk fibroin, hyaluronic acid, and collagen scaffolds have been used in cartilage tissue engineering.[5,6] For instance, Xue et al. prepared cartilage scaffolds with cartilage sheets of pigs.[7] Chen et al. prepared porous cartilage scaffolds using silk fibroin.[8] Browe et al. prepared cartilage scaffolds with customizable shapes using the 3D-printed extracellular matrix.[9] This kind of scaffold has good biocompatibility. Nevertheless, these materials are associated with certain problems, including

insufficient mechanical properties, high degradation rate, and complex modification.[10]

Cartilage scaffolds need to have suitable pores for chondrocyte growth, and their interconnected internal structure should meet the requirements of cell metabolism and waste removal. Implantation in space-limited joints requires compression−expansion deformations of scaffolds to meet minimally invasive treatment. Furthermore, the shape of the scaffold should be customizable to match the surrounding tissue according to the patients' needs.[11] Several articular cartilage scaffolds with internal pores have been prepared by 3D printing, electrospinning, foaming, and other processes using synthetic polymers as raw materials.[1,12] Although these scaffolds have good biological and mechanical properties, they always lack the customization capability in order to match the defects or deformations required for minimally invasive implantation.

Fortunately, 4D printing technology based on shape memory polymers (SMPs) offers viable ideas for addressing
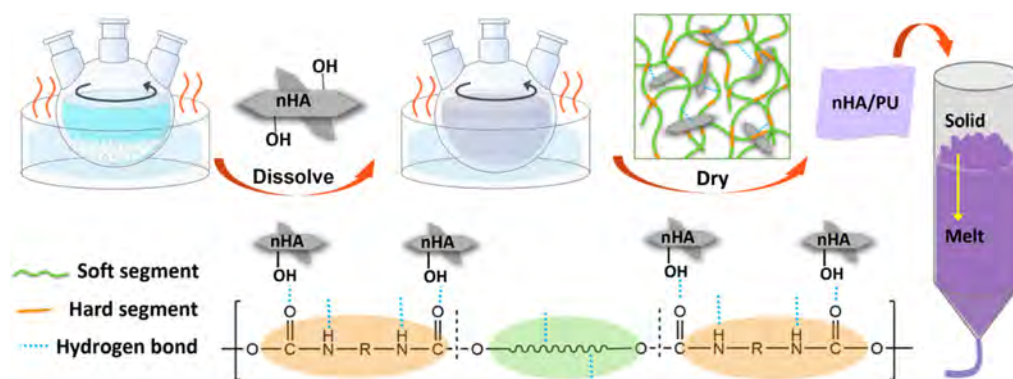
Figure 1. Schematic diagram of the HP composite preparing process.

the urgent need for personalized precision treatment and minimally invasive surgery for cartilage defects.[13,14] In general, 4D printing refers to the additive manufacturing technology that adds a time dimension to 3D printing, which allows the construction of precise and complex smart structures and has become the next-generation solution for tissue engineering.[15,16] SMPs can spontaneously recover from a temporary shape to a permanent shape under external stimulation, including heat,[17,18] light,[19,20] solutions,[21] electrical fields,[22] and magnetic fields.[23] Among them, shape memory polyurethane (SMPU) has been widely used in the biomedical field because of its good biocompatibility and shape memory properties.[24] The polyester chain segments in the SMPU molecules are more flexible and called the soft segment, and the carbamate chain segment is called the hard segment due to its significantly higher stiffness. By adjusting the proportions of soft and hard segments in the SMPU molecular chain, the transition temperature (T_{trans}) and mechanical properties can be easily regulated according to the implantation requirements.[25−27] SMPU with excellent toughness shows a significant advantage in the repair of cartilage defects because articular cartilage needs to withstand alternating stress constantly. However, the construction of 4D printed SMPU structures by FDM technology requires the preparation of uniform printed filaments, and the process is relatively cumbersome.[28] SLA technology has strict requirements on the photocuring properties of materials.[29]

In this paper, a series of shape memory composites (nHA/SMPU, HP) for cartilage defects were prepared by adding nanohydroxyapatite (nHA) into the SMPU matrix (Figure 1a). Various tests were conducted to determine the thermal, mechanical, and shape memory properties. The rheological properties of the HP composite melts had been systematically studied in order to precisely control the printing parameters, ensuring that the construction of 4D printed structures can be realized in a simple, clean, and safe way. Microscopic images showed high-precision and high-quality printing results of the printed filaments. Based on the structural characteristics of mangrove trees, a bionic 4D printed cartilage scaffold was designed, which displayed an adequate shape memory performance in a temperature environment close to that of the human body (Figure 1b). The recovery process was simulated in ABAQUS software to further verify the shape memory performance. 4D printed cartilage scaffolds based on the shape memory composites provide a novel idea for the personalized and minimally invasive treatment of cartilage defects.

2. EXPERIMENTAL SECTION

2.1. Preparation of nHA/PU Composites. Polycaprolactone diol (PCL-OH, 10 g) with a molecular weight of 2000 (2202, Hunan Juren Chemical Hitechnology Co.,Ltd., China) was added into a three-mouth flask and vacuumized for 3 h at 120 °C. Then, 2.6 g of hexamethyldiisocyanate (HDI, Aladdin Reagent (Shanghai) Co., Ltd., China), 20 g of *N,N*-dimethylformamide (DMF), and 0.5 g of dibutyltin dilaurate (Aladdin Reagent (Shanghai) Co., Ltd., China) as a catalyst were added for a 3 h reaction at 90 °C in a nitrogen atmosphere. Subsequently, 0.9 g of 1, 4-butandiol (BDO, Aladdin Reagent (Shanghai) Co., Ltd., China) and 30 g of DMF were added into the mixture for a 2 h reaction. The SMPU films were obtained by drying the mixture in a draught cabinet. The PCL-OH molecular chains are soft segments, and the carbamate chain segment formed by BDO and HDI is the hard segment (Figure 1). Subsequently, four groups of 10 g PU films were dissolved in 20 g of DMF at 70 °C. 0.5, 1, 1.5, and 2 g of nHA powder (Xi'an Ruilin Biological Technology Co., Ltd., China) with a length of 60 nm were added into the PU solution, stirred for 2 h, and then were ultrasonically shaken for 2 h (Figure 1a). Transmission electron microscopy (TEM) images show that the nHA in the mixture is evenly distributed and has no apparent agglomeration (Figure S1). Four groups of the homogenized mixture are poured into a mold and dried in a draught drying cabinet for 12 h to obtain the HP05, HP10, HP15, and HP20 films.

2.2. Characterization. The chemical bonds of PU, HP05, HP10, HP15, and HP20 were characterized by attenuated total reflection Fourier transform infrared spectroscopy (Spectrum One, PerkinElmer, US). The spectral range was 4000−650 cm^{-1}, and the resolution was 4 cm^{-1}. The X-ray diffractometer (XRD, X′ PERT, Panalytical, Netherlands) was used to assess the crystallinity of PU and HPs. The samples were smooth films with dimensions of $20 \times 20 \times 1$ mm. The scanning speed was 5°/min, and the 2θ angle range was between 10 and 80°. A differential scanning calorimeter (DSC1, Mettler-Toledo, Switzerland) was utilized to obtain the endothermic curves of PU and HPs under a heating rate of 5 °C/min from 0 to 120 °C. The mass of the samples ranged within 6−10 mg. Thermal degradation was determined by thermogravimetric analysis (TGA/DSC1, Mettler-Toledo, Switzerland) at a heating rate of 8 °C/min in a flowing nitrogen atmosphere. Tensile tests were performed on a universal testing machine Zwick/Roell Z010 (Zwick GmbH & Co. KG). The tensile specimens were cut according to the standard ASTM D638, type IV. The displacement rate and prestress were 5 mm/min and 0.05 MPa, respectively. The relaxation experiments were conducted on a dynamic thermomechanical analyzer (Q800, TA Instruments, USA). The dimensions of all samples were $40 \times 5 \times 0.5$ mm, and the strain was set as 10%. The surface morphology of printed filaments was observed by scanning electron microscopy (SEM, JSM-7600F, JEOL, Japan) at a voltage of 20 kV. For the U-shaped samples for shape memory recovery test, the material was cut into strip samples with dimensions of $50 \times 5 \times 0.5$ mm, heated to 45 °C, and then fitted to a U-shaped mold with a bending radius of 3 mm for shape rendering.
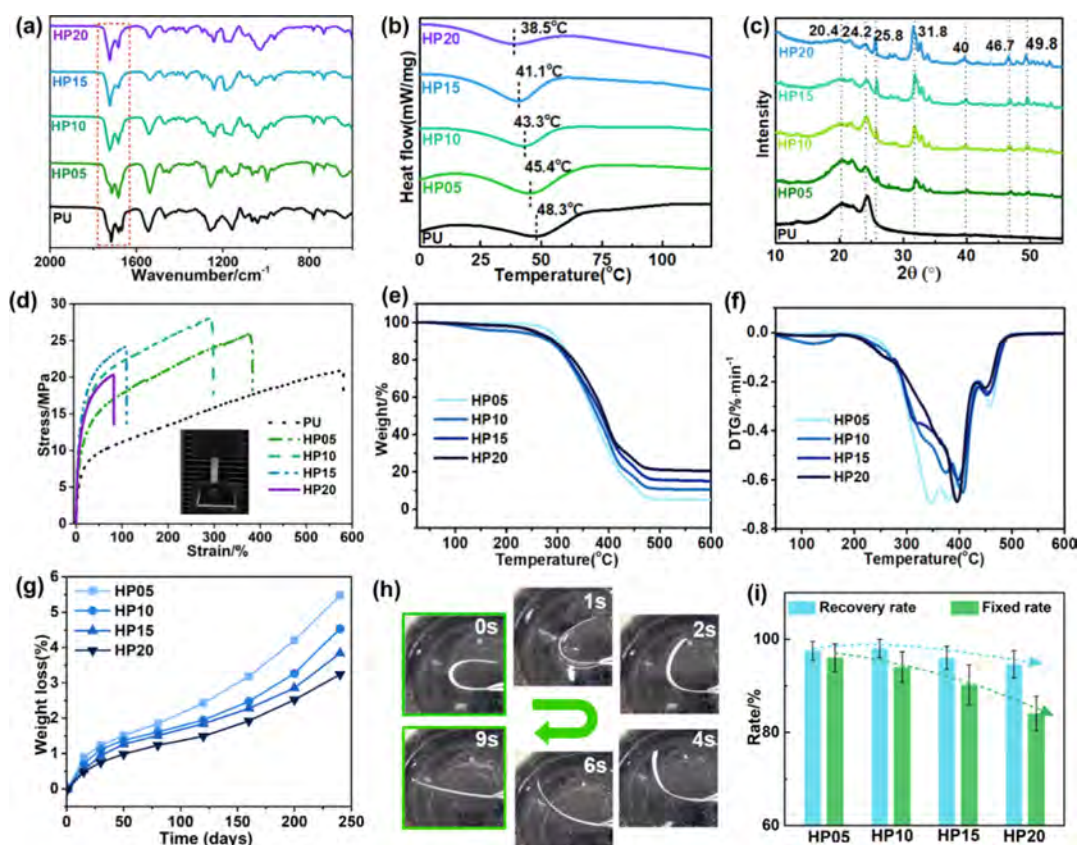
Figure 2. (a) FI-TR spectra of the PU, HP05, HP10, HP15, and HP20 samples. (b) DSC curves. (c) XRD spectra. (d) Tensile stress−strain curves. (e) TGA curves. (f) DTG curves obtained from a derivative of the TGA curves. (g) Degradation curve *in vitro*. (h) Shape recovery process of the HP10 strip at 45 °C. (i) Shape recovery and fixation rates.

2.3. Fabrication of 4D Printed Structures. The 4D printed structures were modeled in Solidworks software and fabricated using the high-temperature printing mode of a 3D-Bioplotter (3D-Bioplotter, EnvisionTEC, USA). First, the model was sliced in Perfactory RP software, and the height of each layer was set as 0.32 mm. After assembling the barrel with a 0.4 mm-diameter needle, the isolated composite specimens were put into the barrel and preheated at 140 °C to the melting state that can be smoothly extruded. Finally, the following printing parameters were set as follows: printing temperature of 140 °C, extrusion pressure of 1.5 bar, printing speed of 9 mm/s, and shell thickness of 0.2 mm.

2.4. *In Vitro* Degradation. The HP composites were cut into rectangular samples with dimensions of 10 × 10 × 0.5 mm. The samples were weighed and placed into sealed Erlenmeyer flasks filled with Hanks solution (Fuzhou Feijing Biological Technology Co., Ltd., China) and then placed into a shaker incubator at a temperature of 37 °C. The samples were taken out at intervals, washed, and vacuum-dried to constant weight. Subsequently, the samples were placed again in the flasks with fresh Hanks solution. The experiment lasted 8 months. The percentage of weight loss (ω_l) was calculated using

$$\omega_l = \frac{m_0 - m(t)}{m_0} \times 100\%$$

(1)

where $m(t)$ is the weight of the specimen at time t after degradation and m_0 is the original weight before degradation.

2.5. Cytocompatibility. Primary fibroblasts were cultured in Dulbecco's modified Eagle's medium containing 10% calf serum and 100 U/mL penicillin/streptomycin in a humidified atmosphere with 5% CO_2 at 37 °C. The HP films with a thickness of 0.5 mm were cut into wafers with a diameter of 5 mm, which were subsequently sterilized with 75% absolute ethanol for 3 h and washed with phosphate buffer saline. Approximately 10^5 primary fibroblasts were co-incubated with the HP wafers in a humidified incubator with 5%

CO_2 at 37 °C. After seeding for 1, 2, and 3 days, the live (stained green) and dead (stained red) cells were observed using a fluorescence microscope (Olympus, Tokyo, Japan). The fibroblast viability was counted and calculated by importing the fluorescence images into ImageJ software.

2.6. Histocompatibility. The experiments were approved by the Medical Ethics Committee of the 2nd Affiliated Hospital of Harbin Medical University. The document number was SYDW2021-110. A total of 18 female C57BL/6 rats weighing 25−28 g were randomly divided into six groups. To facilitate the experimental operation and observe the tissue growth after porous structure implantation, the HP composite was printed into porous wafers with a diameter of 8 mm and a thickness of 1 mm using a bioprinter. After anesthetizing, the HP wafers were implanted subcutaneously into experimental rats. Subsequently, the rats were euthanized at 2, 3, 4, 6, 8, and 12 weeks after the operation. Adjacent tissues of each sample were collected for histological analysis and embedded in paraffin by fixing in 4% paraformaldehyde overnight at 4 °C. Then, the tissues were cut into slices with a thickness of 4 μm using a tissue slicer (RM2235, Leica, Germany). The slices were mounted on glass slides, stained with the hematoxylin−eosin kit (WLA051A, China), and then observed by light microscopic examination (DP73, OLYMPUS, Japan).

3. RESULTS AND DISCUSSIONS

3.1. Properties of nHA/PU Composites. The characteristic groups of the reaction products can be verified by Fourier infrared spectroscopy. As shown in Figure 2a, there is no stretching vibration absorption peak of the isocyanate group (N═C═O) near 2273 cm^{-1} in the PU spectrum, indicating that all HDI had participated in the synthetic process.[30] The peak at 1717 cm^{-1} is formed from the hydrogen-bonded carbonyl group between the soft segment and hard segment.
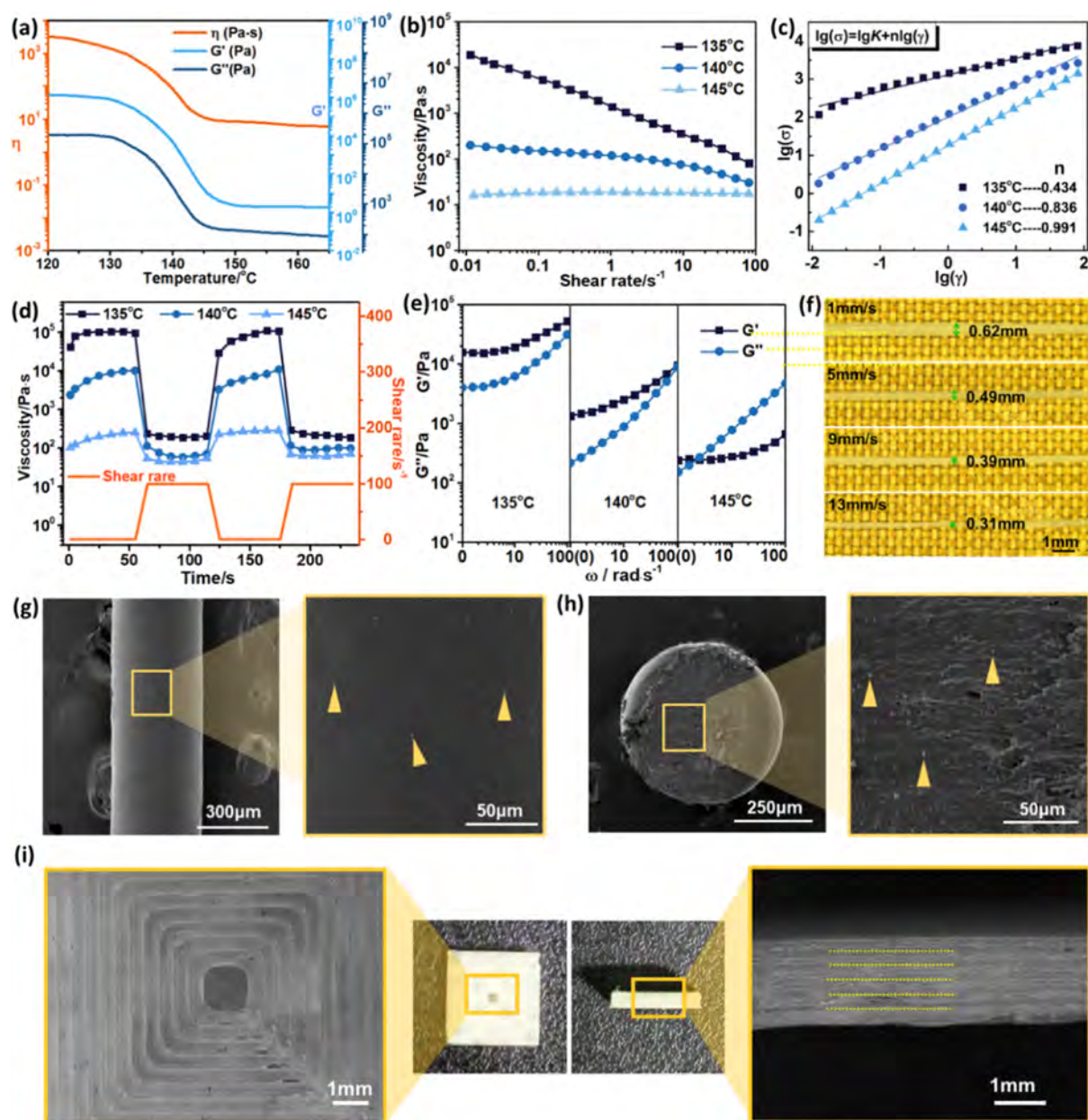
Figure 3. (a) Viscosity curves with temperature under the steady state and G' and G'' curves with temperature in the oscillation mode of the HP melt. (b) Shear viscosity-shear rate curves plotted in the logarithmic coordinate under the steady state at 135, 140, and 145 °C. (c) Logarithmic shear stress *vs* shear rate curves. (d) Viscosity curves under alternating low-high-low shear rates. (e) G' and G'' curves with frequency. (f) Printed filaments extruded with a printing speed of 1, 5, 9, and 13 mm/s under a pressure of 1.5 bar. (g) SEM images of the surface of the printed filament surface. (h) SEM images of a section of the printed filament. (i) 4D printed cuboid and its structural details.

The peak at 1686 cm^{-1} is formed from the free carbonyl group in the carbamate group. The peak at 1668 cm^{-1} is formed from the hydrogen-bonded carbonyl group in the micro-region of the soft segment. The hydrogen bonds in HP composites mainly include four types: the first is the hydrogen bond formed by the carbonyl group in the carbamate group and the hydrogen on the amino group in the SMPU matrix. The second is the hydrogen bond formed by the amino hydrogen in the carbamate group and the carbonyl group in the PCL-OH chain segment in the SMPU matrix. The third is the hydrogen bond formed by the carbonyl group in the PCL-OH chain segment and hydroxyl hydrogen on the nHA surface. The fourth is the hydrogen bond between the carbonyl group in the carbamate group and the hydroxyl hydrogen on the surface of

the nHA. The first and second types can be identified by the characteristic peaks at 1717 and 1668 cm^{-1} in the infrared spectra. Regarding the HP composite, the third and fourth types can be reflected by the reduction of free carbonyls at 1686 cm^{-1} in the infrared spectra. The hydrogen bonds formed between the nHA and PU matrix contribute to the uniform dispersion of nHA and promote the mechanical properties.

In the DSC curves of the HP composite (Figure 2b), the peaks between 38 and 46 °C are generated from the crystallization melting behavior of the soft segments in the PU matrix. The peak value (T_{trans}) decreases with increasing nHA content. The nanoparticles affect the order of soft segments and then affect the crystallization, resulting in a reduction of the crystallization melting temperature. The

crystallization characteristics can also be reflected in the XRD spectra. In Figure 2c, diffraction peaks ranging from 25.8 to 49.8° shown in the spectra of HP05 to HP20 are associated with nHA. Peaks at 20.4 and 24.2° correspond to the PCL crystal, which are unobvious in the HP20 curve. The crystallinities of PU and HP composites were calculated based on the XRD spectra (Table S1). It can be observed that the higher the nHA content, the lower the crystallinity of the samples. The PCL-OH used to prepare the SMPU is prone to crystallization due to its high regularity and good flexibility, but the crystallinity of PCL-OH as the soft segments of SMPU would reduce, since its motion is restricted by the nano-particles.[31]

The addition of nHA has a significant effect on the mechanical properties. As shown in Figure 2d, the elongation at break (ε_m) of the PU matrix reaches more than 500%, exhibiting an excellent toughness. The hydrogen bonds between molecules ensure that the molecules are difficult to separate when subjected to large deformation. The ε_m of HP05 and HP10 with proper amount of nHA decreases, but the strength increases significantly because the nHA particles entangle some molecular chain segments and hinder the slipping. However, the tensile strength and ε_m of HP20 both decrease, which may be due to the agglomeration of excessive nHA and the decreasing crystallinity. Particle agglomeration is prone to stress concentration, which leads to failure acceleration. In addition, nHA affects the thermal stability. At 600 °C, HP20 has the highest residual mass rate (Figure 2e), and the DTG curves obtained from one derivative of TGA curves show that PH05 enters the rapid degradation stage at the earliest (Figure 2f), indicating that nHA can improve the thermal stability. Biodegradability is necessary for the bio-logical material implanted into the body without secondary removal. The degradation experiments of HP composites *in vitro* for 8 months show that all the HP samples maintain the structural integrity for 130 days and subsequently enter a rapid degradation stage (Figure 2g). HP20 shows the slowest degradation speed, which may be related to the hydrophobicity of nHA.

The shape memory performance of HP composites was assessed by bending the straight strips into a "U" shape upon heating above T_{trans} (Figure S2). During this process, the temperature was monitored in real time by the thermocouples. In the case of HP10, it expanded from the "U" shape (temporary shape) to a flat shape (permanent shape) within 10 s upon reheating to 45 °C (Figure 2h). As shown in Figure 2i, HP05 and HP10 have recovery and fixation rates above 90%. The increase in nHA amount leads to a significant decrease in the fixation rate, since it leads to less crystallization, causing insufficient fixation force on the temporary shape. It can be deduced that an appropriate amount of nHA can maintain excellent shape memory performance while improving mechanical properties. Consequently, HP10 was used in the later printing and research work. Then, the shape recovery and fixed rates of HP10 under different temperatures (T_{trans}, T_{trans} +2 °C, T_{trans} +4 °C, and T_{trans} +6 °C) were tested and calculated and are shown in Table S1. It can be observed that at higher temperatures, the shape recovery and fixation rates were higher, and the recovery speed was faster. Subsequently, the HP10 sample was then placed at 20 °C for 20 days to test prolonged fixed rates. As shown in Figure S3, the fixed rate increases significantly at the first and second days, and then, the increased speed slows down and finally reached a stable

state, indicating that the material has good continuity after shape change.

3.2. Design on Printing Parameters. The direct writing 4D printing of the HP composite melt by a bioprinter can simplify the printing process and ensure security for biological applications. Therefore, it is necessary to characterize the rheological properties of the HP melt to accurately control the printing parameters and construct 4D printing structures with various complex configurations. Viscosity is an important index to measure rheological properties, since it represents the internal friction caused by the fluid's flow force. It quantifies the property of preventing the flow within a fluid and the degree of its resistance to the flow. In the printing process, an appropriate viscosity is the main factor ensuring the fluid support transfer and uniform transfer and guarantees that the printing process can proceed smoothly. The printed process of HP melt can be roughly described as follows: first, the HP composite was heated into a molten state in the barrel, and then, the melt was extruded through the nozzle by applying pressure. Subsequently, the extruded print filaments were arranged to form complex structures according to a preset path.[32]

The storage modulus G' with temperature in the oscillation mode and the viscosity η with temperature in the static mode were tested to determine the appropriate printing temperature range. As shown in Figure 3a, the viscosity curve exhibits a significant decrease between 130 and 145 °C because the HP changes from the solid to liquid phase. In the oscillation mode, the storage and loss modulus curves with temperature also show a significant decrease between 130 and 145 °C. Three temperature points (135, 140, and 145 °C) corresponding to about 1/3, 2/3, and 3/3, respectively, of the melting transition process were selected for the following tests. The shear-thinning characteristic is necessary for HP melt to be extruded smoothly through a thin nozzle.[33] As shown in Figure 3b, the viscosity curves decrease with increasing shear rate, exhibiting obvious shear-thinning characteristics, which are conducive to extrusion printing. The relationship between viscosity and shear rate in the logarithmic coordinate is close to linear, so that the relationship can be expressed by the power-law model

$$\eta(\dot{\gamma}) = K \cdot \dot{\gamma}^{n-1} \qquad (2)$$

where K represents material parameters. n is the non-Newtonian exponent, which can be obtained by the Ostwald−Dewaele equation

$$\ln \sigma = \ln K + n \ln \dot{\gamma} \qquad (3)$$

The shear stress and shear rate obtained from the tests were plotted logarithmically. As shown in Figure 3c, the slopes of the three data groups can be obtained by linear fitting, which are n values of HP melt at 140, 144, and 148 °C, which are 0.434, 0.836, and 0.991, respectively. n is less than 1, indicating that the melt is a pseudoplastic fluid.

The HP melt has a low shear rate in the barrel, a high shear when it passes through the nozzle, and a low shear when it is squeezed out from the nozzle. Therefore, fast response to alternating shear rate is necessary for the melt to ensure that the melt can quickly recover structural strength after extruding from the nozzle,[33] which can be tested by a thixotropy test. As shown in Figure 3d, the viscosity maintains a low level in the high shear-rate stage and rapidly increases to a high level when the shear rate is alternating to the low shear-rate stage, indicating that the melt has a rapid response to shear-rate
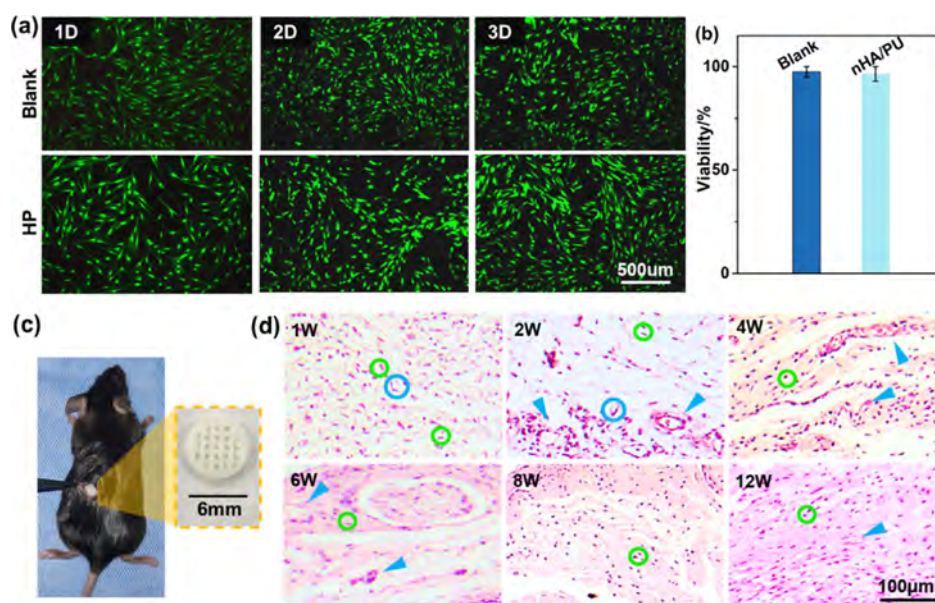
Figure 4. (a) Fluorescent images of the fibroblast cells co-cultured with HP for 1, 2, and 3 days (living cells: green and dead cells: red). (b) Cell viability after 3 days. (c) Subcutaneous implantation of the HP wafers into rats. (d) H&E-stained adjacent tissues of the HP wafers after implantation for different durations (fibroblast cells: green circles; newly formed micro-vessels: blue circles; and blood vessels: blue arrowheads).

changes, which results from the self-repair of physical cross-linking points of the network structure.[34] Subsequently, the printed temperature was determined by frequency scanning tests. The ratio of G' to G'' reflects the ratio of elasticity to viscosity of the material.[35] As shown in Figure 3e, G' is much larger than G'' in the frequency range of 1−100 Hz at 135 °C, indicating that the melt exhibits significant solid-like characteristics.[36] At 145 °C, G' is significantly higher than G'', indicating that the melt has no sufficient strength to support the structure and fix the shape. At 140 °C, the melt has moderate solid-like characteristics, which can maintain the shape of the printed filament without undergoing deformation and has a certain fluidity to ensure the smooth extrusion process.

Three groups of printed pressures (1.5, 2, and 2.5 bar) were set to determine the appropriate printing parameters based on the selected printed temperature and nozzle. The printed filaments were extruded at speeds of 1, 5, 9, and 13 mm/s at a temperature of 140 °C and a pressure of 1.5 bar. As shown in Figure 3f, the width of the printed filament extruded at 9 mm/s is closest to the nozzle diameter (0.4 mm). A too slow printed speed leads to too thick print filaments, while a too fast printed speed leads to more defects. Similarly, printed filaments were extruded under four printed speeds at pressures of 2 bar and 2.5 bar (Figure S4). Using statistics, it was found that the three most appropriate sets of printed parameters at 140 °C were (1.5 bar, 9 mm/s), (2 bar, 12 mm/s), and (2.5 bar, 14 mm/s). An excessive printing speed may reduce the accuracy of printed details, so (1.5 bar, 9 mm/s) was selected for printing. According to the SEM images, the surface of the printing filament is slippery, indicating a smooth extrusion process (Figure 3g). SEM images with high magnification show uniformly distributed nHA particles (yellow arrows). The section of the printed filament is a complete circle, indicating that the printed filament has no transverse deformation during the extrusion process (Figure 3h). In the high-magnification SEM image of the section, it can also be observed that the nHA particles are evenly distributed in the printed filament, indicating that no apparent aggregation of nHA occurred in the

extrusion process. A 4D printed cuboid with dimensions of 10 × 10 × 2 mm was manufactured based on the optimized printing parameters. As shown in Figure 3i, the arrangement of the printed lines along the horizontal plane on the 4D printed cuboid is clear and regular. Along the thickness direction, the printed layers with uniform thickness can be clearly observed, indicating that the HP melt has a good printed effect through the direct-writing technology.

3.3. Biocompatibility. Biocompatibility is necessary for a biological scaffold that can be safely implanted into the human body. Here, the cytocompatibility of HP was evaluated by *in vitro* co-culture of fibroblasts *in vitro*. The fluorescence images of fibroblasts after 1, 2, and 3 days of co-culture with HP are shown in Figure 4a. After 1 day, the density of living cells stained green was relatively low and no obvious dead cells stained red was observed. The number of living cells increased obviously after 2 days. After 3 days, several dead cells can be observed due to the reduction of living space caused by the significant increase in cell density. Compared to the blank group, the number of living cells in the HA group is slightly higher due to the addition of HP. As shown in Figure 4b, the cell viability after 3 days of the HP group is more than 95%, indicating that the HP composite has good cell compatibility and is conducive to endothelization after implantation.

The HP composite was 4D printed into some porous wafers to implant in rats to assess histocompatibility. This method can simulate the acute and chronic self-preservation responses of a foreign porous body after implantation.[37] As shown in Figure 4c, the HP wafers were implanted subcutaneously into rats to assess histocompatibility. The adjacent tissues of wafers after implantation with different durations were collected to monitor the histological condition and then were subsequently stained by standard hematoxylin and eosin (H&E) staining and observed under a microscope. As shown in Figure 4d, the tissue around the wafers is covered with fibroblasts (green circles), accompanied by neovascularization (blue circles) at 1 to 2 weeks. Similar to the wound healing process, angiogenesis plays a vital role in the proliferative phase response, providing a
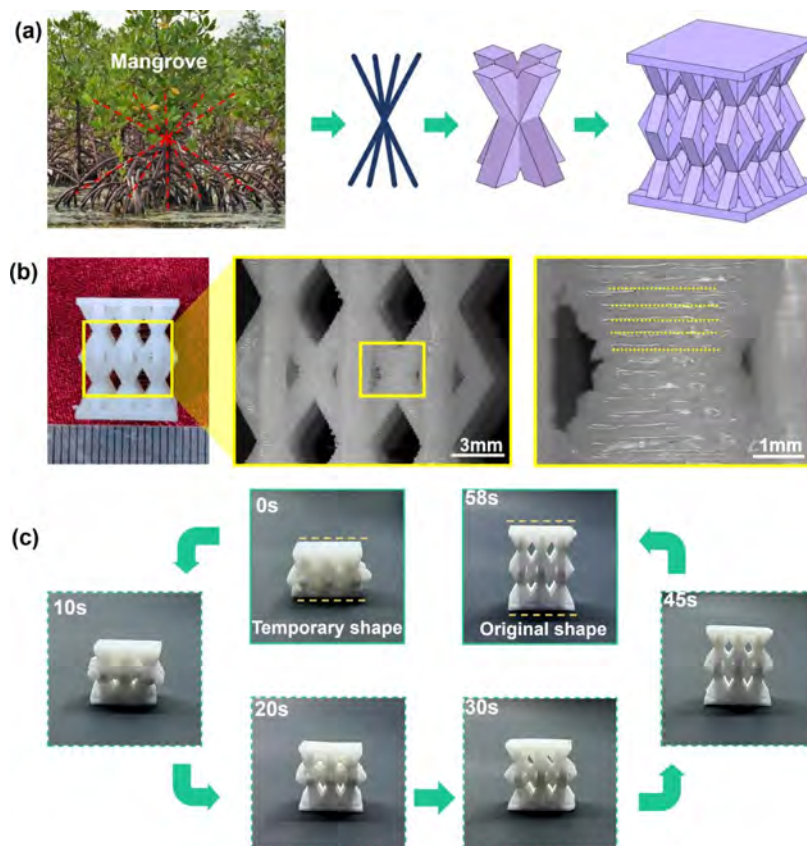
Figure 5. (a) Bionic 4D printed cartilage scaffold inspired from the mangrove structure. (b) 4D printed bionic cartilage scaffold and its structural details. (c) Shape recovery process of the bionic 4D printed cartilage scaffold at 45 °C.

conduit for tissue oxygenation, nutrients, and cell trafficking to facilitate tissue regeneration.[38] After 4 weeks, the young granulation tissues completely covered the wafer entirely. Large vascularity in the tissue (blue arrow) indicates that the tissue growth was in good condition. In summary, the HP wafers exhibit good *in vivo* histocompatibility after implantation.

3.4. 4D Printed Cartilage Scaffold. In subtropical and tropical areas, mangrove forests are effective natural wave attenuation structures due to their dense vegetation and high elevation.[39] The unique structure of a mangrove enables it to grasp the ground steadily and weaken the storm waves effectively, exhibiting excellent mechanical properties.[40] Inspired by the mangrove structure, a structural unit of a bionic articular cartilage scaffold was designed based on the structural characteristics of mangroves (Figure 5a). A cartilage scaffold with an internal connected structure was developed by arraying in Solidworks software. The obtained cartilage scaffold profile is illustrated in Figure S5. The height of each structural unit was set as b, the cross section of the beam was square with a side length of a, and the beam angle was 60°. The shape variation of the scaffold is closely related to the a and b values. Here, the values of a and b were 1.4 and 7 mm, respectively.

Subsequently, a 4D printed cartilage scaffold was manufactured by direct writing of the HP composite melt based on the designed parameters, which shows a good print quality (Figure 5b). The shape recovery process of the cartilage scaffold was performed in a visualized heating furnace with the temperature set to 45 °C. The scaffold was compressed into a temporary shape with a smaller volume by heating and applying pressure;

then, the temporary shape was fixed by cooling. As shown in Figure 5b, the scaffold expanded and returned to its initial shape within 60 s when reheated to 45 °C, which is significant for minimally invasive treatment of cartilage defects. In the treatment process, the scaffold can be compressed into a shape with a smaller volume for convenient implantation. Subsequently, it can expand under thermal stimulation to become a temporary platform for cartilage defect treatment after implantation in the wound. Moreover, the 4D printed cartilage scaffold compressed into temporary shape was placed at 20 °C for 20 days for testing prolonged fixed rates. As shown in Figure S6, the shape fixed rate of the scaffold increases significantly within the first 2 days; then, the increased speed decelerated and finally tends to a stable state, indicating that the deformed scaffold has a good lasting performance.

To predict the shape expansion behavior in the cartilage defect, the shape recovery process of the 4D printed cartilage scaffold was simulated in ABAQUS software. The shape recovery behavior of SMPs is essentially derived from the stress relaxation caused by viscoelasticity.[13] As shown in Figure 6a, the relaxed modulus decreases faster at a high temperature. More relaxation time is required to achieve the same relaxation modulus at low temperatures, indicating that the thermoviscoelastic behavior of the HP composite is temperature-dependent and can be accelerated with the increase in temperature. Eight relaxation curves were plotted in logarithmic coordinates for further analysis (Figure 6b). Taking a temperature of 318 K as the reference temperature value (T_r), the remaining seven relaxation curves can be translated into relaxation curves under a unified reference
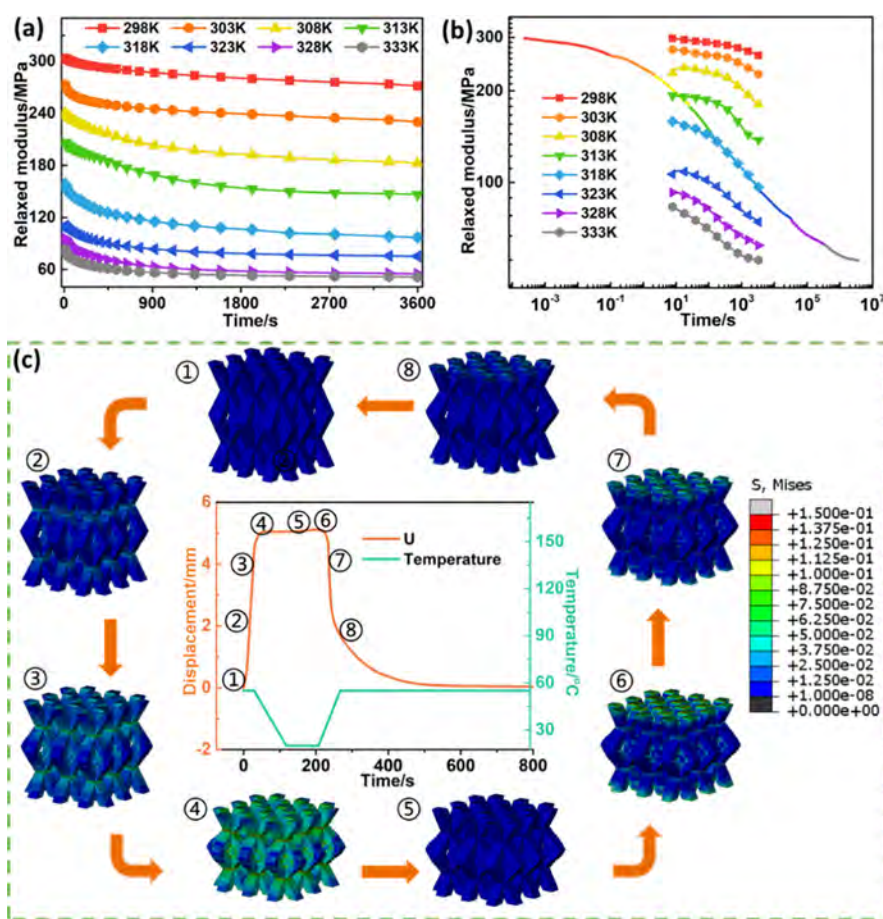
Figure 6. (a) Stress relaxation curves of the HP composite at different temperatures. (b) Stress relaxation curves in logarithmic coordinates and main relaxation modulus curve at 318 K. (c) Simulated shape recovery process of the 4D printed cartilage scaffold.

temperature according to the time−temperature equivalence principle. The main relaxation modulus curve at 318 K can be obtained. Afterward, the Prony series required for the simulation of the shape recovery process in ABAQUS software can be fitted and derived. The detailed derivation and calculation procedures are provided in the Supporting Information.

The lower surface of the scaffold model was fully fixed, and pressure was applied to the upper surface perpendicular to the surface (along the Z-axis). The displacement of the center position node on the upper surface along the Z-axis was the output. As shown in Figure 6c, the upper surface of the scaffold is gradually extruded and deformed during the heating and loading step, corresponding to states 1−3. The stress distribution cloud diagram shows that the stress increases significantly during the loading process. The temporary shape is fixed by maintaining load and cooling, which corresponds to state 4. The deformation is slightly restored when the external force is removed, corresponding to state 5. When entering the reheating step, the temporary shape gradually returns to the initial shape, which corresponds to states 6−8. According to the displacement curve, the displacement is zero at the initial moment and then returns to zero after one shape memory cycle, indicating that a complete recovery has achieved and the shape recovery rate is close to 100%. Overall, the experiment and simulation on the shape memory behaviors of the 4D printed cartilage scaffold demonstrate the feasibility of

minimally invasive treatment for cartilage defects through shape memory properties.

4. CONCLUSIONS

In summary, a 4D printing bionic cartilage scaffold was manufactured by direct-writing bioprinting of HP composite melt, providing a novel idea for personalized and minimally invasive treatment of articular cartilage defects. Thanks to the hydrogen bonds between the nHA surface and the PU matrix, the HP composite possesses good cytocompatibility, histocompatibility, mechanical properties, and shape memory properties. Compared to PU, the strength of HP10 was improved by 200%, and the shape recovery and fixation rates were maintained above 90%. Based on the rheological properties of the composite melt, the printing parameters were precisely optimized and controlled to enable the 4D printing structures with desired shapes. Microscopic images show high printing precision and quality of the printed filaments. Inspired by the structural features of mangroves, a bionic 4D printed cartilage scaffold was designed and manufactured, which can expand from a conveniently insertional shape to a fully expanded shape within 60 s at a temperature close to that of the human body, exhibiting a good shape memory performance. Simulation of the recovery process in software reveals a shape recovery rate close to 100%. The proposed strategy provides ideas for the personalized and minimally invasive treatment of cartilage defects.

■ ASSOCIATED CONTENT

ⓢ Supporting Information

The Supporting Information is available free of charge at https://pubs.acs.org/doi/10.1021/acsapm.2c01833.

TEM images of the HP mixture; schematic diagram of the shape memory test; crystallinity calculated by XRD tests of HP composites; shape recovery rates and fixed rates of HP10 samples at different temperatures; fixed rates of the HP10 sample for 20 days; printed filaments at different speeds; structure parameters of the 4D printed bionic cartilage scaffold; fixed rates of the 4D printed bionic cartilage scaffold for 20 days; scatter diagram of $\lg a(T)$ to temperature T and the fitted curve; main relaxation modulus data and fitted curve; values of E_0 to E_5 when τ_1, τ_2, τ_3, τ_4, and τ_5 are set as 1, 100, 1000, 10000, and 100000, respectively; and fitting values of Prony series (PDF)

■ AUTHOR INFORMATION

Corresponding Author

Jinsong Leng — *Centre for Composite Materials and Structures, Harbin Institute of Technology, Harbin 150000, People's Republic of China;* ⓘ orcid.org/0000-0001-5098-9871; Email: lengjs@hit.edu.cn

Authors

Yongdie Deng — *Centre for Composite Materials and Structures, Harbin Institute of Technology, Harbin 150000, People's Republic of China*

Fenghua Zhang — *Centre for Composite Materials and Structures, Harbin Institute of Technology, Harbin 150000, People's Republic of China*

Yanju Liu — *Department of Astronautic Science and Mechanics, Harbin Institute of Technology, Harbin 150000, People's Republic of China*

Shiqi Zhang — *Department of Ophthalmology, The 2nd Affiliated Hospital of Harbin Medical University, Harbin 150001, People's Republic of China*

Huiping Yuan — *Department of Ophthalmology, The 2nd Affiliated Hospital of Harbin Medical University, Harbin 150001, People's Republic of China;* ⓘ orcid.org/0000-0001-8750-6191

Complete contact information is available at:
https://pubs.acs.org/10.1021/acsapm.2c01833

Notes

The authors declare no competing financial interest.

■ ACKNOWLEDGMENTS

■ REFERENCES

(1) Xuan, H.; Hu, H.; Geng, C.; Song, J.; Shen, Y.; Lei, D.; Guan, Q.; Zhao, S.; You, Z. Biofunctionalized chondrogenic shape-memory ternary scaffolds for efficient cell-free cartilage regeneration. *Acta Biomater.* **2020**, *105*, 97−110.

(2) Huey, D. J.; Hu, J. C.; Athanasiou, K. A. Unlike Bone, Cartilage Regeneration Remains Elusive. *Science* **2012**, *338*, 917−921.

(3) Makris, E. A.; Gomoll, A. H.; Malizos, K. N.; Hu, J. C.; Athanasiou, K. A. Repair and tissue engineering techniques for articular cartilage. *Nat. Rev. Rheumatol.* **2015**, *11*, 21−34.

(4) Pellegrini, V. D.; Guzick, D. S.; Wilson, D. E.; Evarts, M. C. Governance of Academic Health Centers and Systems: A Conceptual Framework for Analysis. *Acad. Med.* **2018**, *94*, 12.

(5) Singh, Y. P.; Bhardwaj, N.; Mandal, B. B. Potential of Agarose/Silk Fibroin Blended Hydrogel for in Vitro Cartilage Tissue Engineering. *ACS Appl. Mater. Interfaces* **2016**, *8*, 21236−21249.

(6) Xue, J.; He, A.; Zhu, Y.; Liu, Y.; Li, D.; Yin, Z.; Zhang, W.; Liu, W.; Cao, Y.; Zhou, G.*Biomedical Materials*; IOP Science: Bristol, England, 2018; Vol. *13*.

(7) Xue, J.; He, A. J.; Zhu, Y. Q.; Liu, Y.; Li, D.; Yin, Z. Q.; Zhang, W. J.; Liu, W.; Cao, Y. L.; Zhou, G. D. Repair of articular cartilage defects with acellular cartilage sheets in a swine model. *Biomed. Mater.* **2018**, *13*, 025016.

(8) Chen, W.; Xu, Y.; Li, H.; Dai, Y.; Zhou, G.; Zhou, Z.; Xia, H.; Liu, H. Tanshinone IIA Delivery Silk Fibroin Scaffolds Significantly Enhance Articular Cartilage Defect Repairing via Promoting Cartilage Regeneration. *ACS Appl. Mater. Interfaces* **2020**, *12*, 21470−21480.

(9) Browe, D. C.; Burdis, R.; Díaz-Payno, P. J.; Freeman, F. E.; Nulty, J. M.; Buckley, C. T.; Brama, P.; Kelly, D. J. Promoting endogenous articular cartilage regeneration using extracellular matrix scaffolds. *Mater. Today Bio* **2022**, *16*, 100343.

(10) Angele, P.; Abke, J.; Kujat, R.; Faltermeier, H.; Schumann, D.; Nerlich, M.; Kinner, B.; Englert, C.; Ruszczak, Z.; Mehrl, R.; Mueller, R. Influence of different collagen species on physico-chemical properties of crosslinked collagen matrices. *Biomaterials* **2004**, *25*, 2831−2841.

(11) Montgomery, M.; Ahadian, S.; Davenport Huyer, L.; Lo Rito, M.; Civitarese, R. A.; Vanderlaan, R. D.; Wu, J.; Reis, L. A.; Momen, A.; Akbari, S.; Pahnke, A.; Li, R. K.; Caldarone, CA.; Radisic, M. Flexible shape-memory scaffold for minimally invasive delivery of functional tissues. *Nat. Mater.* **2017**, *16*, 1038−1046.

(12) Yuan, Z. G.; Long, T.; Zhang, J.; Lyu, Z.; Zhang, W.; Meng, X. C.; Qi, J.; Wang, Y. 3D printed porous sulfonated polyetheretherketone scaffold for cartilage repair: Potential and limitation. *J. Orthop. Translat.* **2022**, *33*, 90−106.

(13) Deng, Y.; Zhang, F.; Jiang, M.; Liu, Y.; Yuan, H.; Leng, J. Programmable 4D Printing of Photoactive Shape Memory Composite Structures. *ACS Appl. Mater. Interfaces* **2022**, *14*, 42568−42577.

(14) Wu, J. J.; Huang, L. M.; Zhao, Q.; Xie, T. 4D Printing: History and Recent Progress. *Chin. J. Polym. Sci.* **2018**, *36*, 563−575.

(15) Lee, J.; Kim, H.; Choi, J.; Lee, I. H.A review on 3D printed smart devices for 4D printing. *International Journal of Precision Engineering and Manufacturing-Green Technology*; Springer, 2017; Vol. *4*, pp 373−383.

(16) Wan, Z.; Zhang, P.; Liu, Y.; Lv, L.; Zhou, Y. Four-dimensional bioprinting: Current developments and applications in bone tissue engineering. *Acta Biomater.* **2020**, *101*, 26−42.

(17) Zhang, Y.; Zhang, N.; Hingorani, H.; Ding, N.; Wang, D.; Yuan, C.; Zhang, B.; Gu, G.; Ge, Q. Fast-Response, Stiffness-Tunable Soft Actuator by Hybrid Multimaterial 3D Printing. *Adv. Funct. Mater.* **2019**, *29*, 1806698.

(18) Liu, Y.; Zhang, W.; Zhang, F.; Lan, X.; Leng, J.; Liu, S.; Jia, X.; Cotton, C.; Sun, B.; Gu, B.; Chou, T. W. Shape memory behavior and recovery force of 4D printed laminated Miura-origami structures subjected to compressive loading. *Composites, Part B* **2018**, *153*, 233−242.

(19) Bai, X.; Yang, Q.; Li, H.; Huo, J.; Liang, J.; Hou, X.; Chen, F. Sunlight Recovering the Superhydrophobicity of a Femtosecond

Laser-Structured Shape-Memory Polymer. *Langmuir* **2022**, *38*, 4645−4656.

(20) Liang, R.; Yu, H.; Wang, L.; Wang, N.; Amin, B. U. NIR Light-Triggered Shape Memory Polymers Based on Mussel-Inspired Iron−Catechol Complexes. *Adv. Funct. Mater.* **2021**, *31*, 2102621.

(21) Xue, J.; Ge, Y.; Liu, Z.; Liu, Z.; Jiang, J.; Li, G. Photoprogrammable Moisture-Responsive Actuation of a Shape Memory Polymer Film. *ACS Appl. Mater. Interfaces* **2022**, *14*, 10836−10843.

(22) Gong, X.; Xie, F.; Liu, L.; Liu, Y.; Leng, L. Electro-active Variable-Stiffness Corrugated Structure Based on Shape-Memory Polymer Composite. *Polymers* **2020**, *12*, 387.

(23) Lin, C.; Lv, J.; Li, Y.; Zhang, F.; Li, J.; Liu, Y.; Liu, L.; Leng, J. 4D-Printed Biodegradable and Remotely Controllable Shape Memory Occlusion Devices. *Adv. Funct. Mater.* **2019**, *29*, 1906569.

(24) Mondal, S. Temperature responsive shape memory polyurethanes. *Polym.-Plast. Technol. Mater.* **2021**, *60*, 1491−1518.

(25) Su, J.-W.; Gao, W.; Trinh, K.; Kenderes, S.; Pulatsu, E.; Zhang, C.; Whittington, A.; Lin, M.; Lin, J. 4D printing of polyurethane paint-based composites. *Int. J. Smart Nano Mater.* **2019**, *10*, 237.

(26) Gupta, A.; Maharjan, A.; Kim, B. S. Shape Memory Polyurethane and its Composites for Various Applications. *APPLIED SCIENCES-BASEL* **2019**, *9*, 4694.

(27) Chan, B.; Low, Z.; Heng, S.; Chan, S. Y.; Owh, C.; Loh, X. J. Recent Advances in Shape Memory Soft Materials for Biomedical Applications. *ACS Appl. Mater. Interfaces* **2016**, *8*, 10070−10087.

(28) Karakurt, I.; Lin, L. 3D printing technologies: techniques, materials, and post-processing. *Current Opinion in Chemical Engineering* **2020**, *28*, 134−143.

(29) Quan, H.; Zhang, T.; Xu, H.; Luo, S.; Nie, J.; Zhu, X. Photo-curing 3D printing technique and its challenges. *Bioact. Mater.* **2020**, *5*, 110−115.

(30) Henry, J. A.; Simonet, M.; Pandit, A.; Neuenschwander, P. Characterization of a slowly degrading biodegradable polyesterur-ethane for tissue engineering scaffolds. *J. Biomed. Mater. Res., Part A* **2007**, *82A*, 669−679.

(31) Yu, G.; Chen, H.; Wang, W.; Zhou, Y.; Zhang, J.; Li, Y. Influence of sepiolite on crystallinity of soft segments and shape memory properties of polyurethane nanocomposites. *Polym. Compos.* **2018**, *39*, 1674−1681.

(32) Zhang, M. S.; Vora, A.; Han, W.; Wojtecki, R. J.; Maune, H.; Le, A.; Thompson, L. E.; McClelland, G. M.; Ribet, F.; Engler, A. C.; Nelson, A. Dual-Responsive Hydrogels for Direct-Write 3D Printing. *Macromolecules* **2015**, *48*, 6482−6488.

(33) Liu, Z. B.; Zhang, M.; Bhandari, B.; Yang, C. H. Impact of rheological properties of mashed potatoes on 3D printing. *J. Food Eng.* **2018**, *220*, 76−82.

(34) Martínez, A.; Ortiz Mellet, C. O.; García Fernández, J. Cyclodextrin-based multivalent glycodisplays: covalent and supra-molecular conjugates to assess carbohydrate-protein interactions. *Chem. Soc. Rev.* **2013**, *42*, 4746−4773.

(35) Liu, H.; Xu, X. M.; Guo, S. D. Rheological, texture and sensory properties of low-fat mayonnaise with different fat mimetics. *LWT−Food Sci. Technol.* **2007**, *40*, 946−954.

(36) Chaisawang, M.; Suphantharika, M. Pasting and rheological properties of native and anionic tapioca starches as modified by guar gum and xanthan gum. *Food Hydrocolloid* **2006**, *20*, 641−649.

(37) Fournier, E.; Passirani, C.; Montero-Menei, C. N.; Benoit, J. P. Biocompatibility of implantable synthetic polymeric drug carriers: focus on brain biocompatibility. *Biomaterials* **2003**, *24*, 3311−3331.

(38) Bodnar, R. J. Anti-Angiogenic Drugs: Involvement in Cutaneous Side Effects and Wound-Healing Complication. *Adv. Wound Care* **2014**, *3*, 635−646.

(39) Menéndez, P.; Losada, I. J.; Torres-Ortega, S.; Narayan, S.; Beck, M. W. The Global Flood Protection Benefits of Mangroves. *Sci. Rep.* **2020**, *10*, 4404.

(40) Bouma, T. J.; van Belzen, J.; Balke, T.; Zhu, Z. C.; Airoldi, L.; Blight, A. J.; Davies, A. J.; Galvan, C.; Hawkins, S. J.; Hoggart, S.; Lara, P. G.; Losada, J. L.; Maza, I. J.; Ondiviela, M.; Skov, M. W.; Strain, M. W.; Thompson, E. M.; Yang, R. C.; Zanuttigh, S. L.; Zhang, B.; Herman, L.; Herman, P. M. J. Identifying knowledge gaps hampering application of intertidal habitats in coastal protection: Opportunities & steps to take. *Coast. Eng.* **2014**, *87*, 147−157.